

Experiments and numerical simulations of Lueders bands and Portevin–Le Chatelier effect in aluminium alloy AW5083

M. MUCHA¹), L. ROSE²), B. WCISŁO¹), A. MENZEL^{2,3}), J. PAMIN¹)

¹) *Chair for Computational Engineering, Cracow University of Technology, Warszawska 24, 31-155 Cracow, Poland, email: Marzena.Mucha@pk.edu.pl*

²) *Institute of Mechanics, Department of Mechanical Engineering, TU Dortmund University, Dortmund, Germany*

³) *Division of Solid Mechanics, Department of Construction Sciences, Lund University, Lund, Sweden*

THIS WORK IS FOCUSED ON THE MODELING OF EXPERIMENTAL BEHAVIOUR OF a bone-shape sample made of aluminium alloy AW5083 under tension. This behaviour involves propagating instabilities, namely Lueders bands and the Portevin–Le Chatelier effect. A series of experiments was performed at room temperature for three loading rates, showing the instabilities and failure. In the paper a large strain thermo-visco-plasticity model is proposed and used for finite element simulations. This model contains initial softening and a hardening function based on the Estrin–McCormick concept to represent serrations and travelling shear bands. The issues of instability sources and regularisation are considered. The predictive capabilities of the model are examined. The proposed models are able to reproduce both Lueders bands and the PLC effect. Simulation results show good agreement with experiments regarding force–displacement diagrams and temperature levels.

Key words: Lueders bands, PLC effect, aluminum alloy, large strains, thermo-visco-plasticity.



Copyright © 2023 The Authors.

Published by IPPT PAN. This is an open access article under the Creative Commons Attribution License CC BY 4.0 (<https://creativecommons.org/licenses/by/4.0/>).

1. Introduction

SOME TECHNOLOGICALLY IMPORTANT MATERIALS, for instance steel or aluminium alloys, can exhibit propagative instability phenomena, namely Lueders bands and/or the Portevin–Le Chatelier (PLC) effect. The instabilities can lead to material degradation and have a negative influence on the material performance, leading to faster failure. They can be observed in a certain range of strain rates and temperatures. They can have a transient or recurring character and they can occur during one process, see for example [1].

The aim of the paper is to present the numerical simulation of the experimentally observed response of dog-bone aluminium specimens in tension. The experiments are performed at room temperature, but three loading rates are ex-

amed. In each case both the transient Lueders phenomenon and the recurring PLC-type instabilities are observed. The numerical analysis of the experiments is performed with a finite strain thermo-visco-plasticity model. In the model the yield function, which involves strain-rate softening, is based on the concept of McCormick [2]. The comparison of the results of experiments and simulations serves the purpose of verification of the numerical model.

The first description of Lueders bands was published as early as 1860 in [3]. In a metal sample, after the onset of yielding some softening can occur and then a stationary shear band is formed. When the material in the band starts to harden, on its edge a plastic front forms and the band moves through the sample, which is associated with a plateau in the force–displacement diagram. When the band reaches the opposite end of the sample, a hardening phase with uniform deformation in the whole sample is observed. More information about Lueders bands propagation can be found for instance in [4].

The Portevin–Le Chatelier effect was first described in [5]. Repetitive changes from hardening to softening and again to hardening called serrations are then present in the force–displacement diagrams. The stress jumps are associated with the formation and movement of a localisation band in the sample or with the band decay and reappearance at a different place. The PLC effect is commonly related to the so-called Dynamic Strain Aging (DSA) which is in turn related to the negative strain rate sensitivity of a material. At the microscopic level the plastic flow in metals can be explained by the motion of dislocations. This motion can be stopped by solute atoms or other dislocations, causing a dislocation pile-up. When the stress grows sufficiently, the dislocations are freed and the process can repeat itself. More information about the micro-mechanical origin of the PLC effect can be found for instance in [6], while the DSA was already discussed in [7, 8].

Several studies regarding the Lueders bands and the PLC effect are available in the literature. Most experiments showing Lueders bands are performed on samples loaded under tension, for example in [9], but also in shear [10, 11] and in bending [12–14]. The materials that exhibit this kind of behaviour are steel [15, 16] and aluminum alloys [17, 18], but also shape-memory alloys [19, 20]. The PLC effect occurs in aluminum alloys at room temperature [21, 22] and in steels at elevated temperature [23, 24], but also in Nickel-based alloys [25]. The PLC bands can be observed both in tension [26] and in shear [10, 27]. At temperatures close to absolute zero a process similar to the Dynamic Strain Aging can also occur [28].

For some materials Lueders bands and the PLC effect can appear during one process (first the Lueders bands and then the PLC effect), see [1, 29]. In a few studies the two effects are considered together in the investigation of Al-Mg [10, 30] and steel [31]. Figure 1 in [1] presents load-elongation diagrams obtained for α -iron for the strain rate equal to $9.7 \cdot 10^{-4}$ 1/s and different temperatures

(57 degrees to 329 degrees Celsius). For lower temperatures a clear Lueders plateau is visible followed by saturation hardening. When the temperature increases, PLC serrations start to show and when the temperature exceeds 300 deg Celsius the serrations disappear and the Lueders plateau is hardly visible. In [29] a similar phenomenon can be observed for aluminium alloy 5456Al for the strain rate equal to $5.4 \cdot 10^{-4}$ 1/s and temperatures ranging from 173 K to 333 K. A broad review of experimental findings concerning the PLC effect can be found in [32].

Different models have been used to simulate the propagative instability phenomena, but full thermo-mechanical coupling has rarely been considered. In [33] a multi-linear hardening approach (softening and then hardening) for the Lueders bands and negative strain rate for the PLC effect are adopted in the algorithm of wave propagation. A model which is a phenomenological description of DSA was proposed by McCORMICK [2]. In the model an additional variable, called strain aging time, is used to introduce repetitive strain rate softening and hardening phases. Typical plots showing how the strain aging time depends on the increasing deformation are shown in [34]. The approach, also called the Estrin–McCormick model, was later extended by other authors, for instance [35–39]. A different model based on thermodynamic features was proposed in [40, 41]. Numerical aspects of the finite element (FE) analysis of the PLC effect, including the strain rate sensitivity, is presented in [42].

In the present paper experiments conducted on dog-bone samples, made of aluminium alloy AW5083 and loaded under tension, are compared with numerical simulations performed using large strain thermo-visco-plasticity. The experiments are carried out for three (average) strain rates: $4.3 \cdot 10^{-2}$, $4.3 \cdot 10^{-3}$ and $4.3 \cdot 10^{-4}$ 1/s with three repetitions for each considered strain rate. During the experiments the strain distribution is monitored by using a DIC system and the temperature distribution is recorded with a thermal imaging camera. The thermo-plastic model [43, 44] augmented to include the rate-dependence (a viscous term and a recurring strain-rate softening term) is used. A multi-linear softening-hardening model for Lueders bands and the Estrin–McCormick relations for the PLC effect are employed. The model includes full thermo-mechanical coupling with thermal expansion, thermal softening in the yield function, plastic heating, and Fourier’s law formulated in the current configuration. The Huber–Mises–Hencky definition of equivalent stress is applied in the so-called consistency visco-plasticity formulation, proposed in [33] and now employed in the formulation for finite deformations.

The Lueders bands model was considered by the authors in [45] and the Estrin–McCormick model was employed in the simulation study of PLC bands presented in [34]. Here, the models are combined and equipped with additional switch functions to turn on and off the parts of the description. Optionally, a gradient-enhancement in the form of temperature averaging is taken into ac-

count. The models are implemented by using the AceGen code generator to profit from the possibility of automatic differentiation, and computations are performed in the AceFEM which is an FE environment within the Wolfram Mathematica, see [46].

The paper is organised as follows. Section 2 provides an overview of the experiments. In Section 3 a brief description of the constitutive model is presented. Section 4 contains both the experimental and computational results. Force–displacement plots and temperature evolution at the middle point of the sample are compared, as well as temperature and strain distributions in the sample. Section 5 presents a summary and conclusions with some prospect of future work.

2. Experiments

The experiments which are used for the verification of the proposed model are introduced in this section. At first, the specimens are presented, followed by the testing and measuring devices. Afterwards, the experimental procedure is briefly explained and, finally, the obtained force, displacement and temperature data are shown and analysed. It is worth mentioning that the aim of the experiments at this stage is simply to verify the ability of the model to represent the plastic instability effects of Lueders and PLC bands. Thus, simple tension tests were chosen as the basis of this proof of concept, in order to single out the desired effects and thereby avoid different material effects, which might be introduced by more elaborate experiments.

2.1. Specimens

The experiments were performed at the Institute of Mechanics, TU Dortmund University, using specimens made of the aluminium alloy AW5083. All samples were water cut from a sheet metal plate with an orientation of zero degrees between the tension axis and the rolling direction of the plate. The chosen geometry can be seen in Fig. 1; it is based on DIN 50125 for simple tension tests.

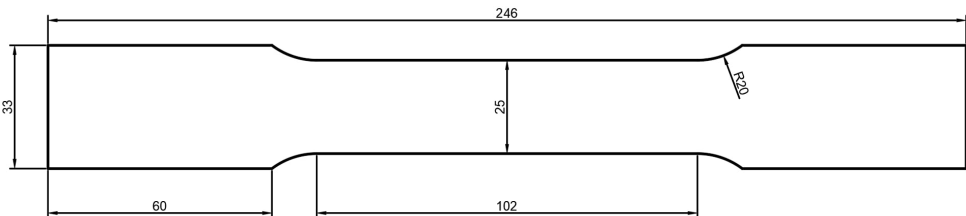


FIG. 1. Sample shape and dimensions in mm. Thickness of the specimen is 2 mm.

2.2. Experimental setup

In order to later compare temperature as well as force and displacement data from experiments and model predictions, the respective data is obtained by using the Digital Image Correlation (DIC) system Aramis with 4 Mpx from GOM, as well as the thermography (TG) system ImageIR 8320hp from InfraTec. The use of both systems requires a speckle pattern to be applied to one side of each specimen and a homogeneous black coating with a known emission coefficient which is applied to the other side prior to testing. It is worth mentioning that this specific TG system measures electro-magnetic waves with a wavelength between 2.0 and 5.7 μm (medium-wavelength-window). In this bandwidth, the emission coefficients of most paints vary significantly, so that it is not possible to place both systems on the same side of the specimen. Hence, the two systems must be placed on opposing sides. After clamping the specimens and waiting for an initial steady temperature state, the specimens were loaded displacement controlled with a constant rate of the cross head until failure, using the tensile machine LFM 100-T200 from Walter + Bai with a nominal load of 100 kN. More precisely speaking, three different rates were used to gain a first impression about the rate dependence of the plastic instabilities and to verify the model's ability to capture this dependence. While the constant displacement rate of the cross head does not lead to a constant strain rate within the specimen, a rough estimate of the average strain rate can nevertheless be made, see Table 1 and Fig. 2. Although it

TABLE 1. Loading rates and average strain rates of the experiments.

Experiment No.	Displacement rate [mm/s]	Average strain rate [1/s]
1, 2, 3	0.06	$4.3 \cdot 10^{-4}$
4, 5, 6	0.60	$4.3 \cdot 10^{-3}$
7, 8, 9	6.00	$4.3 \cdot 10^{-2}$

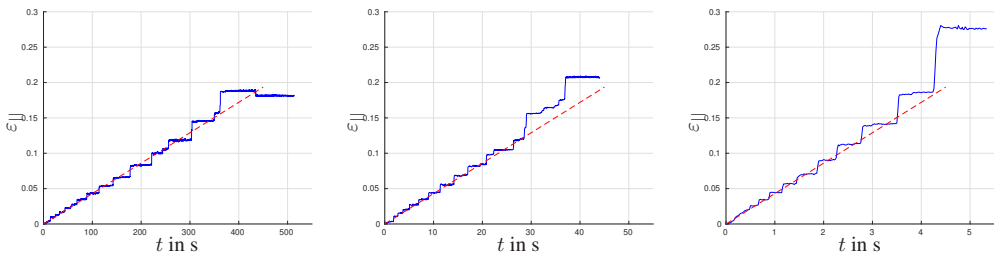


FIG. 2. Local engineering strain in tension direction (—) at the centre point of the specimen and estimated average strain (---) versus time for representative experiments with low, medium and high strain rates (left to right).

is well established that the PLC effect is not only strain rate but also temperature dependent, all experiments were performed at room temperature for this initial proof of the concept.

2.3. Experimental data

An initial analysis of observed effects is performed in this section by showing mainly the local point data versus time. Further details of the full field data can be found in Section 4, where experimental data is compared to the predicted results of a simulation.

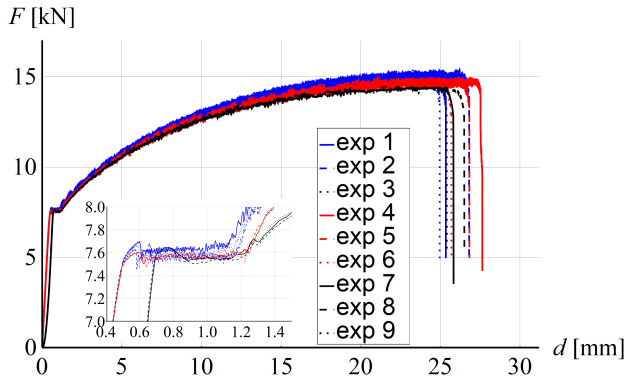


FIG. 3. Force versus cross head displacement of the tension machine. Maximum load capacity decreases with increasing strain rate. Numbers (exp no.) in legend indicate numbering of respective experiment, cf. Table 1.

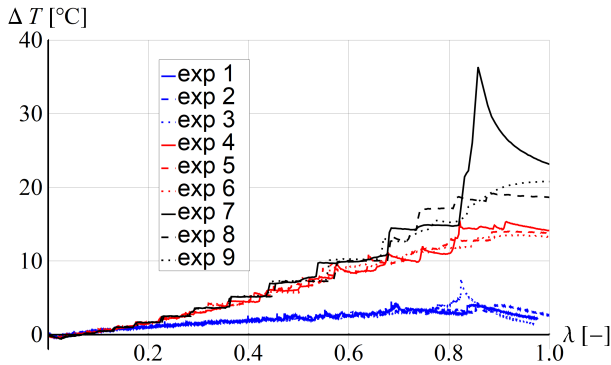


FIG. 4. Temperature increase at centre point of specimen versus load factor λ which increases from 0 to 1 with imposed elongation (enabling presentation of all diagrams in one figure). Numbers (exp no.) in legend indicate numbering of respective experiment, cf. Table 1.

Elastic response. The initial mechanical material behaviour appears to be linear elastic and independent of the chosen strain rates, as can be seen by the parallel initial force–displacement curves in Fig. 3. The slight offset of the black curves (highest strain rate) is probably rather due to the impulse-like start of the experiment, leading to a slight initial slip, than induced by a viscous response of the material. Although no unloading stage was incorporated to verify the claim of elasticity, the drop in temperature due to the elastic Gough–Joule effect likewise indicates elastic material behaviour, see Fig. 4.

Initial plastic response – Lüders bands. The plastic response of the material starts with a sharp drop in reaction force and a classic, albeit small Lüders plateau. The shear bands are clearly visible in the DIC and thermography images. It is worth mentioning that all dissipative processes like the movement of an already existing band or the appearance of a new band is always related to an increase in local temperature, such that the tracking of active bands is slightly simpler in the TG images, cf. Fig. 5, at least for materials with a rather high thermal conductivity. Furthermore, the point in time of initial plastification

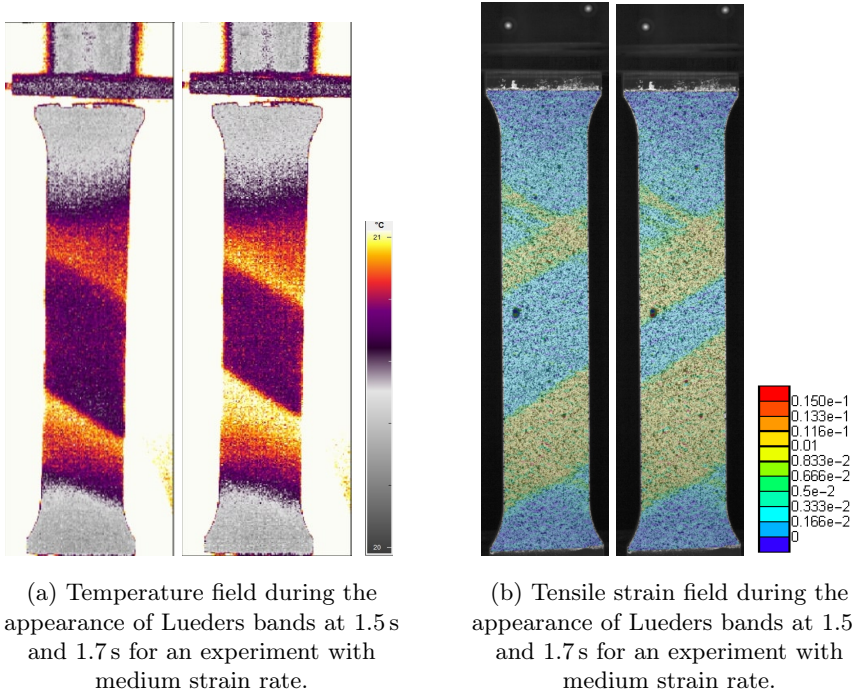


FIG. 5. Lüders bands as observed by TG (a) and DIC (b) system. Active band fronts can better be identified using a TG system. The TG system is positioned opposite the DIC system, which explains the seemingly different orientations of bands.

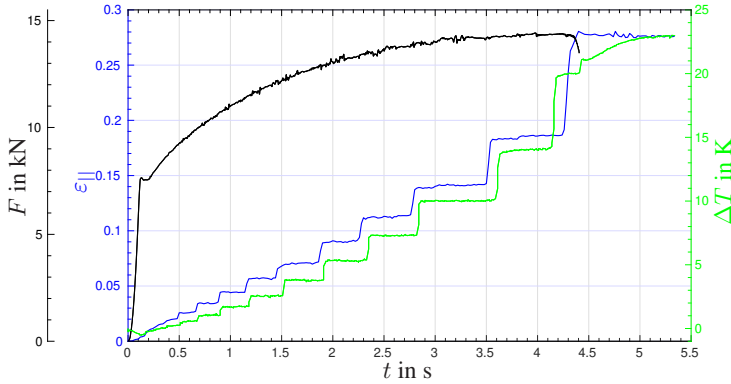


FIG. 6. Global reaction force, local engineering strain in tension direction and local temperature increase at the centre point of the specimen versus time for a representative experiment with high strain rate. Temperature increase starts with the onset of plasticity and the initial drop in reaction force.

can therefore also be determined by observing whether the temperature of the specimen starts to increase (at some material point, i.e. the location of the first Lüders band), see e.g. Fig. 6.

Plastic response – PLC bands. The material response following the Lüders plateau is characterised by overall, non-linear plastic hardening as well as by the appearance of PLC bands. As in the previous case, the PLC effect is clearly visible in the serrated force–displacement curves, see Fig. 3, as well as in the DIC and TG images, see Figs. 16 and 18. A close analysis shows that the bands not only propagate through the entire sample, but that new bands appear at seemingly random locations, propagate some random distance, sometimes switch orientation or disappear again. Comparing the force–displacement diagrams for different strain rates in Fig. 3 shows that the amplitude of the serrations as well as the overall load capacity decreases with an increasing strain rate. Especially, the latter effect appears counter-intuitive at first, since viscosity would usually lead to an increase of forces. However, the complex material effects within the alloy at hand lead to an overall reduction of the maximum applicable force with increasing strain rate. This effect is not necessarily related to the strain rate alone, but can also be related to a change in temperature and thermal softening, which is caused by the increase of the strain rate, allowing less time for the heat to flow.

Material response close to failure. At some elevated loading stage, one of the currently active bands further localises and a macro crack appears along the re-

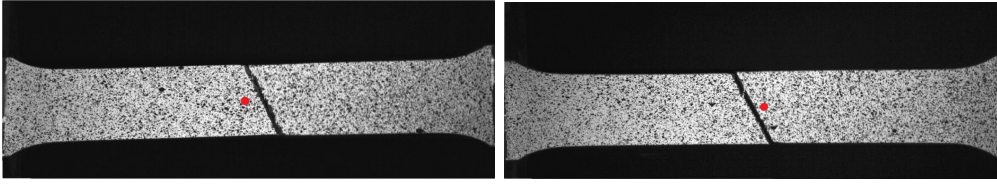


FIG. 7. Final failure mode with sample centre marked by red dot for samples no. 3 and 7.

spective shear band, see Figs. 7, 18 and 16. The macro crack evolves very rapidly, i.e. the specimen exhibits (quasi) brittle damage failure at room temperature.

The exact position of failure cannot be determined a priori and depends, for instance, on micro defects and further imperfections of each sample. The same is true for the final ductility of the material, prior to failure, which differs for almost all experiments, see Fig. 3. Hence, a comparison of the obtained data with a deterministic model is only reasonable up to a certain loading stage. This can also be seen in the local temperature data of Fig. 4, which is almost identical for all experiments of a certain strain rate, but tends to differ significantly close to the stage of cracking, since the position of the crack and the dissipation source related to its formation is different for all experiments.

With this data at hand, a model is proposed in the following, which captures some of the main effects observed. Furthermore, the experimental data is used to verify the ability of the proposed model to represent the desired features.

3. Modelling framework

In this section essential aspects of the model proposed are summarised. This includes the specification of the thermomechanically coupled constitutive relations as well as aspects of regularisation and implementation.

3.1. Material model

The analysed aluminium sample is modelled by using geometrically non-linear thermo-elasto-plasticity based on [47, 48]. The material description presented in this section is an extension of the model used in [34] for simulations of the PLC effect.

We consider a deformable continuous body consisting of isotropic material. Every particle of the body is denoted with the vector \mathbf{X} in the referential (initial) configuration and with the vector $\mathbf{x}(\mathbf{X}, t)$ in the current placement at time t . The deformation gradient and its multiplicative decomposition are given as follows:

$$(3.1) \quad \mathbf{F} = \frac{\partial \mathbf{x}}{\partial \mathbf{X}}, \quad \mathbf{F} = \mathbf{F}^e \mathbf{F}^p \mathbf{F}^\theta,$$

where \mathbf{F}^e , \mathbf{F}^p and \mathbf{F}^θ represent the elastic, plastic and thermal parts of deformation, cf. [48]. The last part related to thermal expansion of the material is assumed to be purely volumetric and is defined as:

$$(3.2) \quad \mathbf{F}^\theta = [J^\theta]^{1/3} \mathbf{I}, \quad J^\theta = \det(\mathbf{F}^\theta) = \exp(3\alpha_T[T - T_0]),$$

where α_T is the linear thermal expansion coefficient, T denotes the temperature of the particle and T_0 denotes its reference (initial) temperature. Moreover, \mathbf{I} represents the second order identity tensor.

It is assumed that the Helmholtz free energy, which is a function of the elastic left Cauchy–Green deformation tensor $\mathbf{b}^e = \mathbf{F}^e[\mathbf{F}^e]^T$, hardening variable α and temperature T , is additively decomposed into elastic, plastic and thermal parts, i.e.

$$(3.3) \quad \psi(\mathbf{b}^e, \alpha, T) = \psi^e(\mathbf{b}^e) + \psi^p(\alpha) + \psi^\theta(T).$$

The elastic part is specified in the following form

$$(3.4) \quad \psi^e(\mathbf{b}^e) = \frac{1}{2}G \left[[J^e]^{-2/3} \text{tr}(\mathbf{b}^e) - 3 \right] + \frac{1}{2}K \ln(J^e)^2,$$

where $\text{tr}(\bullet)$ denotes the trace of tensor \bullet , $J^e = \det(\mathbf{F}^e) > 0$ is the determinant of the elastic part of the deformation gradient, while G and K are the elastic shear and bulk moduli, respectively. The plastic part of the free energy function $\psi^p(\alpha)$ depends on the applied plastic hardening description, see also Appendix A, whereas the purely thermal part is assumed in a classical form, cf. [47], resulting in a constant heat capacity.

The yield function is written in terms of the Kirchhoff stress tensor

$$(3.5) \quad \boldsymbol{\tau} = 2 \frac{\partial \psi^e}{\partial \mathbf{b}^e} \mathbf{b}^e$$

and is defined as follows

$$(3.6) \quad F_p(\boldsymbol{\tau}, \alpha, \dot{\alpha}, T) = f(\boldsymbol{\tau}) - \sqrt{\frac{2}{3}} \sigma_y(\alpha, \dot{\alpha}, T) \leq 0,$$

where $f(\boldsymbol{\tau})$ is a stress measure which defines the yield surface and $\sigma_y(\alpha, \dot{\alpha}, T)$ represents the evolving yield strength dependent on the hardening variable, its rate $\dot{\alpha}$ and temperature. In particular, the Huber–Mises–Hencky (HMH) stress measure is applied:

$$(3.7) \quad f(\boldsymbol{\tau}) = \sqrt{2J_2}, \quad J_2 = \frac{1}{2} \boldsymbol{\tau}_{dev}^2 \cdot \mathbf{I}, \quad \boldsymbol{\tau}_{dev} = \boldsymbol{\tau} - \frac{1}{3} \text{tr}(\boldsymbol{\tau}) \mathbf{I}.$$

The associative flow rule applied in the model has the following form, cf. [47, 49],

$$(3.8) \quad -\frac{1}{2}\mathcal{L}_v\mathbf{b}^e = \dot{\gamma}\mathbf{N}^p\mathbf{b}^e,$$

where $\mathcal{L}_v\mathbf{b}^e$ denotes the Lie derivative of the elastic left Cauchy–Green deformation tensor, $\mathbf{N}^p = \partial F_p/\partial \boldsymbol{\tau}$ is the normal to the yield surface and $\dot{\gamma}$ is the plastic multiplier. The description is completed with the Kuhn–Tucker loading–unloading conditions for plastic multiplier $\dot{\gamma}$ and yield function F_p , i.e.:

$$(3.9) \quad \dot{\gamma} \geq 0, \quad F_p \leq 0, \quad \dot{\gamma}F_p = 0.$$

The relation between the rate of hardening variable and the plastic multiplier is $\dot{\alpha} = \sqrt{2/3}\dot{\gamma}$.

The yield strength for the employed thermo-visco-plastic model consists of three contributions, i.e.

$$(3.10) \quad \sigma_y(\alpha, \dot{\alpha}, T) = \sigma_H(\alpha, T) + \sigma_V(\dot{\alpha}) + \sigma_B(\alpha, \dot{\alpha}).$$

The first one represents linear strain hardening, saturation hardening and thermal softening in the following form

$$(3.11) \quad \sigma_H(\alpha, T) = [\sigma_{y0} + S_1(\alpha)H\alpha + S_2(\alpha)S_3(\alpha)[\sigma_{yf} - \sigma_{y0}][1 - \exp(-\delta\alpha)]] [1 - H_T[T - T_0]],$$

where H is a scalar parameter (positive for hardening and negative for softening), σ_{y0} and σ_{yf} are initial and final yield strengths, respectively, δ is a saturation parameter and H_T is a positive-valued thermal softening modulus. The thermal softening term $1 - H_T[T - T_0]$ in the above equation is non-negative only for particular temperatures ranges, i.e. for $T < T_0 + 1/H_T$. Within the numerical simulations presented in the subsequent sections this inequality is fulfilled. The three quantities $S_1(\alpha)$, $S_2(\alpha)$ and $S_3(\alpha)$ appearing in Eq. (3.11) are switch functions dependent on the hardening variable, which are designed to turn on or off the effect of a selected contribution. The functions are specified by the following formulas:

$$(3.12) \quad S_1(\alpha) = \frac{-\arctan(100[\alpha - \alpha_{LB}])}{\pi} + \frac{1}{2},$$

$$(3.13) \quad S_2(\alpha) = \frac{\arctan(100[\alpha - \alpha_{LB}])}{\pi} + \frac{1}{2},$$

$$(3.14) \quad S_3(\alpha) = \frac{-\arctan(100[\alpha - \alpha_1])}{\pi} + \frac{1}{2}$$

and are illustrated in Fig. 8. The first switch function $S_1(\alpha)$ is used to switch off the linear softening part after reaching α_{LB} (which we call Lueders strain), the

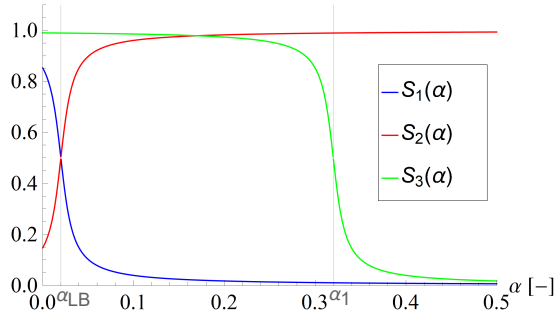


FIG. 8. Values of switch functions vs hardening variable.

second $S_2(\alpha)$ is used to switch on the saturation hardening part after reaching α_{LB} and the third function $S_3(\alpha)$ is used to switch off the hardening after failure threshold α_1 is reached. The switch functions have a continuum character (i.e. they are not step functions) for algorithmic reasons. They allow us to avoid difficulties in automatic differentiation.

The viscoplastic component in Eq. (3.10) follows the consistency concept, cf. [33], and has the following simple form

$$(3.15) \quad \sigma_V(\dot{\alpha}) = \xi \dot{\alpha},$$

where ξ is a scalar viscosity parameter. The rate of the hardening variable $\dot{\alpha}$ is approximated by using the backward Euler integration scheme, i.e. $\dot{\alpha} = [\alpha_{n+1} - \alpha_n]/\Delta t$, where α_{n+1} and α_n are the values of the hardening variable from the current and the previous time steps, respectively, and where Δt is the related time increment.

The last contribution to the yield strength is a macroscopic phenomenological representation of the DSA phenomenon according to McCormick's concept [35, 36] and is based on the model presented in [37], i.e.

$$(3.16) \quad \sigma_B(\alpha, \dot{\alpha}) = S_3(\alpha) \sigma_{B0}(\alpha) \left[1 - \exp \left(- \frac{t_a(\alpha, \dot{\alpha})}{t_0} \right)^m \right],$$

where $t_a(\alpha, \dot{\alpha})$ is the so-called strain aging time which is an additional variable used to represent the PLC effect. Moreover, the saturation coefficient is assumed as a linear function of α , i.e.

$$(3.17) \quad \sigma_{B0}(\alpha) = \sigma_{B00} + \sigma'_{B00} \alpha.$$

In the above equations, σ_{B00} , σ'_{B00} , m and t_0 are model parameters. The last parameter is called the DSA characteristic time. The strain ageing time t_a evolves according to the equation

$$(3.18) \quad \dot{t}_a = 1 - \frac{t_a}{t_w}.$$

The waiting time $t_w(\alpha, \dot{\alpha})$ in the above equation is related to the plastic strain rate in the following way

$$(3.19) \quad t_w = \frac{\Omega(\alpha)}{\dot{\alpha}}, \quad \Omega(\alpha) = \Omega_0 + \Omega'_0 \alpha,$$

where Ω_0 and Ω'_0 are model parameters. Application of the implicit time integration scheme in Eq. (3.18) with Eq. (3.19) leads to the following formula for the value of the strain ageing time at the current time step,

$$(3.20) \quad t_{a,n+1} = \frac{t_{a,n} + \Delta t}{1 + \frac{\Delta \alpha}{\Omega(\alpha_n + \Delta \alpha)}},$$

where $t_{a,n}$ is the value of the strain ageing time at the previous time step. The DSA part of the yield function is switched off by the function $S_3(\alpha)$ when α reaches the failure threshold α_1 . Due to this approach, DSA is not simulated in the post-peak regime, which is consistent with the observed experiments.

As it was mentioned above, the constitutive description presented in this paper is an extension of the thermo-mechanical model formulated in [43, 44] and developed in [34] for the simulation of the PLC effect. It is worth emphasising which modifications of the previous model are now introduced to match the experimental sample behaviour. Firstly, the thermo-visco-plastic McCormick model is combined with the Lueders bands model by adding an initial linear softening part in Eq. (3.11) and the saturation hardening parameters are appropriately adapted. Secondly, the switch functions are introduced in the description in order to reproduce Lueders bands at the beginning of the plastic process and sample failure at the end as well as to prevent extensive serrations in the post peak regime. The combined model with the arctangent switches is able to reproduce the initial Lueders band plateau and the repeated serrations related to the PLC effect together with the final failure.

3.2. Regularisation

The presented model is susceptible to a loss of material stability due to several reasons. Firstly, the Lueders bands observed at the beginning of the plastic process are related to the initial strain softening. Secondly, unstable behaviour is observed at a further stage during the tension process in the form of the PLC effect which manifests itself in the strain rate softening and serrations in the force–displacement diagram. Thirdly, thermo-mechanical coupling involves thermal softening which is represented by a decrease of the yield strength with the temperature growth. All destabilising factors are taken into account in the employed model which can lead to the ill-posedness of the boundary value problem

and to pathological mesh sensitivity in the numerical simulations, cf. e.g. [50]. To avoid this problem a suitable regularisation should be incorporated.

Among different stabilising factors or methods which can be found in the literature, the model proposed in this work includes regularisation introduced by heat conduction [43, 51, 52] and positive rate-dependence in the yield strength (viscosity) [53–55]. Furthermore, in order to provide additional regularisation the model is enriched with higher order temperature gradients according to [43], and $\sigma_H(\alpha, T)$ then becomes

$$(3.21) \quad \sigma_H(\alpha, z) = [\sigma_{y0} - S_1(\alpha)H\alpha + S_2(\alpha)S_3(\alpha) [\sigma_{yf} - \sigma_{y0}] [1 - \exp(-\delta\alpha)]] [1 - H_T z],$$

where z is an averaged relative temperature, computed from the following differential equation

$$(3.22) \quad z - l^2 \nabla_{\mathbf{x}}^2 z = T - T_0$$

with homogeneous natural boundary conditions. Parameter l in the above equation is called the internal length scale and should influence the width of strain localisation zone. It is assumed in this model that the averaging is performed in the reference configuration (cf. [56]), thus the material gradient operator $\nabla_{\mathbf{x}}$ is applied in Eq. (3.22). In particular, this last regularisation is designed as a remedy for thermal softening in the presence of large temperature gradients due to plastic heating. If viscosity and conductivity are treated as material properties, high loading rates may result in semi-adiabatic conditions so that the gradient enhancement stabilises, respectively regularises, the softening processes.

3.3. Implementation

To perform numerical simulations for the presented complex model a user subroutine for the AceGen/FEM finite element environment, see [49], is programmed. The implemented thermo-visco-plasticity with gradient averaging is a three field model with the following nodal unknowns: displacement vector, temperature and non-local variable. The governing equations are the balance of linear momentum,

$$(3.23) \quad J \operatorname{div}(\boldsymbol{\tau}/J) = \mathbf{0},$$

the balance of energy,

$$(3.24) \quad c \frac{\partial T}{\partial t} - J \operatorname{div}(-\mathbf{q}/J) - \mathcal{R} = 0$$

and the averaging Eq. (3.22), each of the equations with relevant boundary conditions. In the governing equations $\operatorname{div}(\cdot)$ denotes spatial divergence, $J =$

$\det(\mathbf{F}) > 0$ is the determinant of the deformation gradient, c is heat capacity and \mathbf{q} is the Kirchhoff heat flux density vector. The heat source \mathcal{R} includes the heat generated during plastic dissipation according to the simplified formula, [48],

$$(3.25) \quad \mathcal{R} = \chi \sigma_y \dot{\alpha},$$

where χ is the Taylor–Quinney factor assumed to be constant and close to 1.

The constitutive relation for the Kirchhoff heat flux is assumed as the isotropic Fourier’s law in the current configuration

$$(3.26) \quad \mathbf{q} = -k \nabla_{\mathbf{x}} T,$$

where k is a scalar conductivity.

The weak forms of the governing equations and the implementation of a similar three-field model in symbolic-numerical software AceGen/FEM are described in detail in [43]. If the additional gradient-type regularisation is not used, the problem reduces to two fields, typical for thermo-mechanics. For the subsequent finite element examples all fields are approximated by linear shape functions and hexahedral elements. In order to avoid volumetric locking for volume-preserving plasticity, the F-bar approach presented in [57] is applied.

Moreover, aspects of thermodynamic consistency of the model are discussed in Appendix A, whereas the local material response predicted by the model proposed is additionally illustrated in Appendix B.

4. Model verification

In this section experimental data are compared with computational results. Integral, local and field data (from DIC and thermography) are used. The parameters for the aluminum alloy AW5083 are given in Table 2. The basic mechanical and thermal parameters $\{\rho, E, \nu, k, c, \alpha_T\}$ are taken from literature. The finite element mesh and boundary conditions are shown in Fig. 9. First, the experimental force–displacement diagrams for different strain rates and the simulated diagrams for the two modelling options, i.e. with (grad) or without (visco) the gradient-type temperature averaging as introduced in Eqs. (3.21) and (3.22), are plotted. The temperature evolution at the centre point for different strain rates and the two models is then compared to the experimental observations. Next, an analysis of the Lueders bands stage of the response is presented, where selected images are shown for experiments and computations. Furthermore, a similar study is performed for serrations occurring during the PLC process. The images of temperature and engineering strain selected from the entire test in equal intervals are compared. Finally, computational images of the distribution of the equivalent plastic strain rate $\dot{\alpha}$ are presented.

TABLE 2. Model and process parameters for aluminium alloy AW5083. In last column the source of data is given (F denotes fitted values).

Property	Symbol	Value	Unit	Source
Young modulus	E	70	GPa	[37]
Poisson ratio	ν	0.3	–	[37]
Initial yield strength	σ_{y0}	110	MPa	F
Final yield stress	σ_{yf}	190	MPa	F
Saturation constant	δ	19.618	–	F
Linear hardening modulus	H	$-0.005 E$	GPa	F
Viscosity	ξ	40	MPa·s	F
Internal length	l	5	mm	F
Heat conductivity	k	121	J/[s·K·m]	[58]
Heat capacity	c	875	J/[kg·K]	[58]
Thermal expansion coeff.	α_T	$23.2 \cdot 10^{-6}$	1/K	[58]
Thermal softening modulus	H_T	0.0016	1/K	F
Heat dissipation factor	χ	0.9	–	[59]
Density	ρ	2660	kg/m ³	[58]
Lueders strain	α_{LB}	0.01	–	F
Failure threshold	α_1	0.33	–	F
EMC model parameter	Ω_0	$12.36 \cdot 10^{-4}$	–	F
EMC model parameter	Ω'_0	$7.2 \cdot 10^{-4}$	–	F
DSA characteristic time	t_0	0.125	s	[37]
EMC model parameter	σ_{B00}	$47.25 \cdot 10^6$	MPa	F
EMC model parameter	σ'_{B00}	$435.3 \cdot 10^6$	MPa	F
EMC model exponent	m	3^{-1}	–	[37]
Enforced displacement	ΔL	31.2	mm	–
Maximum tension time	t_{MAX}	5.2/52/520	s	–
Reference temperature	T_0	20	°C	–

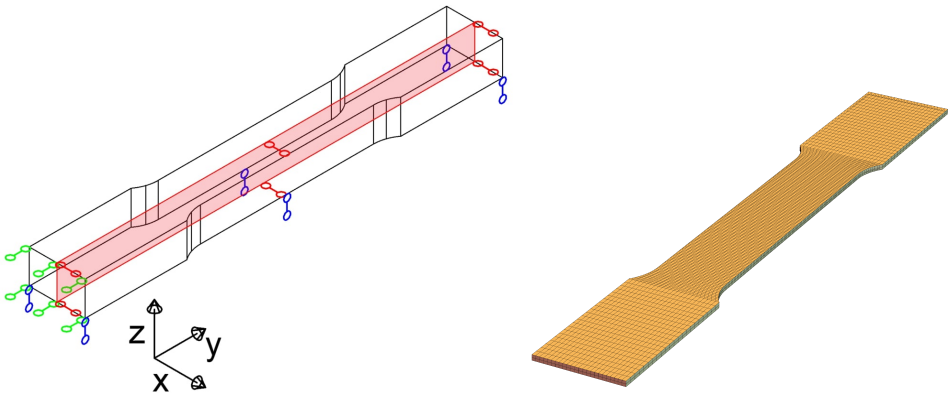


FIG. 9. Illustration of boundary conditions (left); mesh with 7968 finite elements in total and two elements in thickness direction (right).

4.1. Force–displacement diagrams for different loading rates

In Fig. 10 diagrams presenting the sum of reactions versus the sample elongation for the thermo-visco-plastic model with or without gradient enhancement are presented for t_{MAX} equal to 520, 52 and 5.2 s. Numbers 1–9 in the figures are the experimental sample numbers (1, 2, 3 – low strain rate, 4, 5, 6 – medium strain rate, 7, 8, 9 – high strain rate), cf. Table 1. The parameters of the model marked with F in Table 2 have been fitted manually to experimental data for the medium strain rate (t_{MAX} equal to 52 s); therefore the best compatibility of experimental and computed diagrams is seen in Fig. 10, top right.

For all cases brief softening, a short plateau and then saturation hardening are visible, matching the experimental sample behaviour. There are some differences in the shear band propagation process depending on the strain rate, which could be related to the types of PLC effect, but this issue is not examined in the paper. Serrations are visible in the numerical response, but a further adjustment is needed regarding their size and starting point especially for the slow and fast processes. This suggests that a better strain rate and/or temperature dependence of material model components should be worked out in the future research.

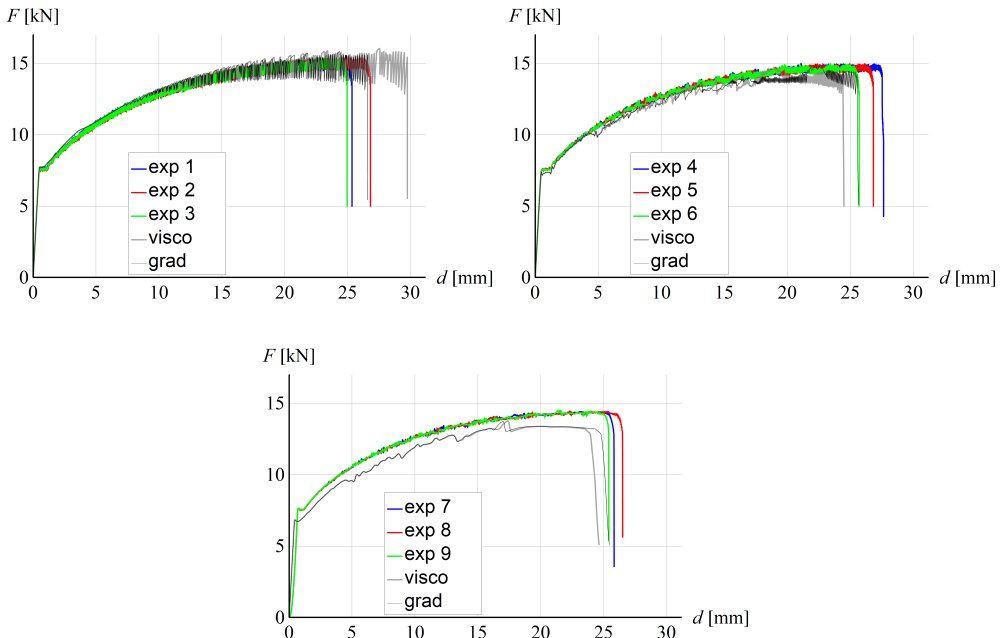


FIG. 10. Sum of reactions vs sample elongation computed for thermo-visco-plastic model and its gradient-enhanced version for $t_{\text{MAX}} = 520$ s (top left), $t_{\text{MAX}} = 52$ s (top right), $t_{\text{MAX}} = 5.2$ s (bottom).

Concerning the regularisation, the diagrams for the thermo-visco-plastic model and for the model with temperature averaging do not differ significantly during the pre-peak phase and the serration sizes are also similar.

4.2. Temperature evolution at selected point for different strain rates

In Fig. 11 the relative temperature at the sample central point in the current configuration is plotted through the whole process, where λ is the elongation multiplier which takes values from 0 to 1 (1 corresponds to the end of the process). For each strain rate, the levels of temperature obtained in experiments and computations are similar. The discrepancies visible in the experimental diagrams for sample numbers 3 and 7 as well as computations for visco-plastic model for the slow process are caused by the fact that the final localisation band is close to the monitored centre point. It can be seen in Fig. 7 where the point is marked by a red dot in the figures of sample numbers 3 and 7. The temperature in that part of the sample is higher, whereas the rest of the sample already cools down. At the beginning of the process a slight temperature drop is visible in the experimental diagrams, most probably caused by the Gough–Joule effect. The drop is not present in the computational diagram – in order to reproduce this effect, the model would have to be extended to include thermo-elastic coupling in the specification of the balance of energy.

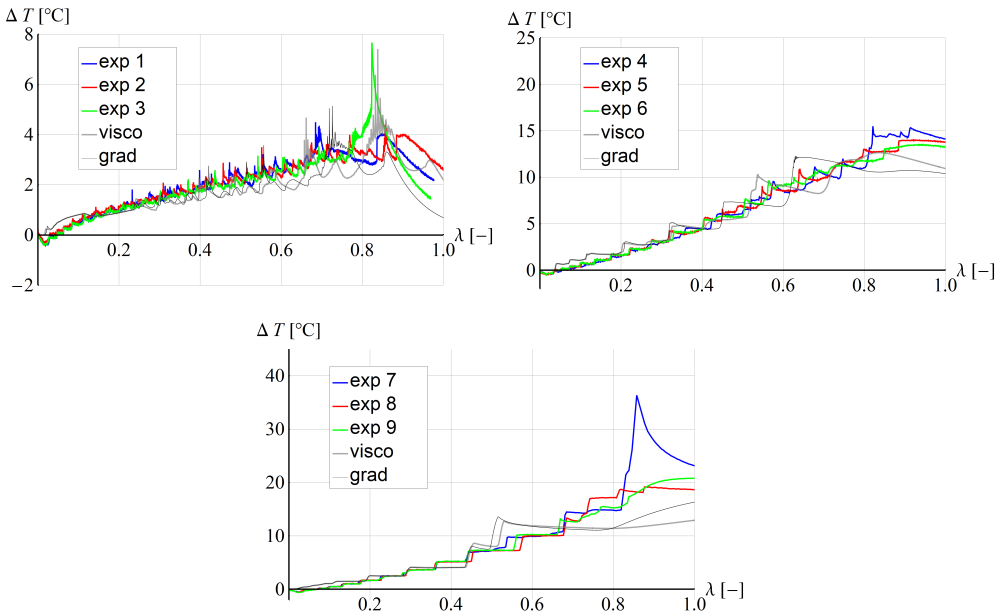


FIG. 11. Relative temperature (ΔT) at the centre of the sample for $t_{MAX} = 520s$ (top left), $t_{MAX} = 52s$ (top right), $t_{MAX} = 5.2s$ (bottom).

4.3. Field analysis of Lueders bands and PLC effect

In Fig. 12 the evolution of experimentally measured longitudinal engineering strain is plotted for sample number 5, selected for a comparison of results. The plots are made in equal intervals, for the following sequence of time moments: 1.1, 1.3, 1.5, 1.7, 1.9, 2.1 s. The time moments are also indicated by green vertical lines in the force–displacement diagrams presented in Fig. 13. A first Lueders-type band is formed in the upper part of the sample (Fig. 12, first image from the left) and evolves together with another band into an (unsymmetric) X-shape pattern. Moreover, one more band is formed in the lower part of the sample (second image from the left). Then one of the upper bands and the lower band start to propagate towards each other (Fig. 12, images 3 and 4 from the left) until they merge (images 5 and 6). A similar process is captured by computations, noting that we compare the distributions of total longitudinal strains and not strain increments (or rates). In Fig. 14 the distribution of longitudinal engineering strain is shown for loading states corresponding to those presented in Fig. 12. First, X-shape band patterns are formed in the top and bottom parts of the sample, see Fig. 14, first image from the left. Then they propagate towards the sample centre and transform into two zones of localised strain, as shown in images 2–5 from the left. In image 6 the bands are fully merged, which is typical for Lueders bands at the hardening stage. It should be mentioned that in computations we observe X-shape bands due to symmetry of the specimen, boundary conditions and discretisation. During the experimental process one of the two bands of the X-shape pattern is dominant due to small imperfections and hence we can observe an unsymmetrical X-shape band at the beginning of the process.

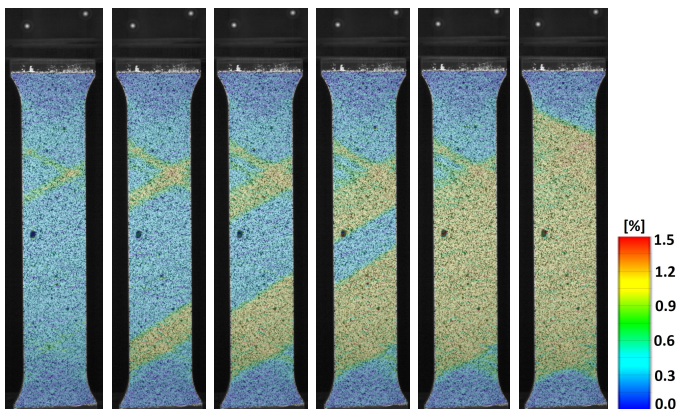


FIG. 12. Evolution of longitudinal engineering strain for experimental sample 5 (medium strain rate) at time moments 1.1, 1.3, 1.5, 1.7, 1.9, 2.1 s from left to right.

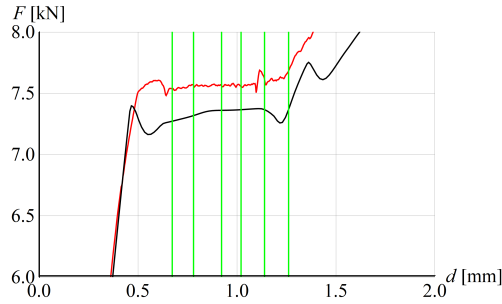


FIG. 13. Sum of reactions vs sample elongation computed for experimental sample 5 (red line) and thermo-visco-plastic model.

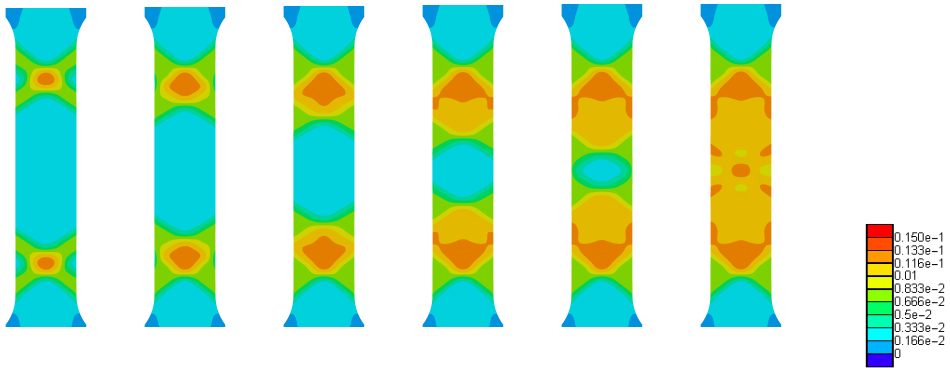


FIG. 14. Distribution of longitudinal engineering strain at selected time moments for thermo-visco-plastic model.

In Fig. 15 force–displacement diagram parts are shown for selected serrations from experiments (left) and computations (right). In the left plot green lines mark points for which longitudinal engineering strains are plotted in Fig. 16 using DIC data. It is visible that bands propagate from the top of the sample (see first five images from the left). In the last image a band jumped to another location close to the centre of the sample.

Turning attention to the modelling, the red points in the right diagram of Fig. 15 mark the steps, for which distributions of the equivalent plastic strain rate $\dot{\alpha}$ are plotted in Fig. 17. This field is used rather than the longitudinal engineering strain in order to obtain better visibility of band formation and vanishing. The first image from the left in Fig. 17, associated with the state between two serrations (at the beginning of local softening branch, see Fig. 15, right), shows an emerging X-shape band pattern in the upper part of the sample, with some residual plastic activity below it. Going down towards the lowest point

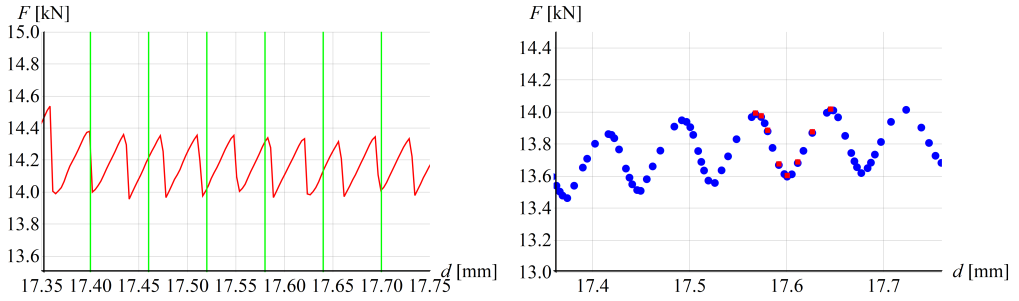


FIG. 15. Zoom of part of diagram showing sum of reactions vs sample elongation for experimental sample 5 (left) and simulation obtained with thermo-visco-plastic model (right).

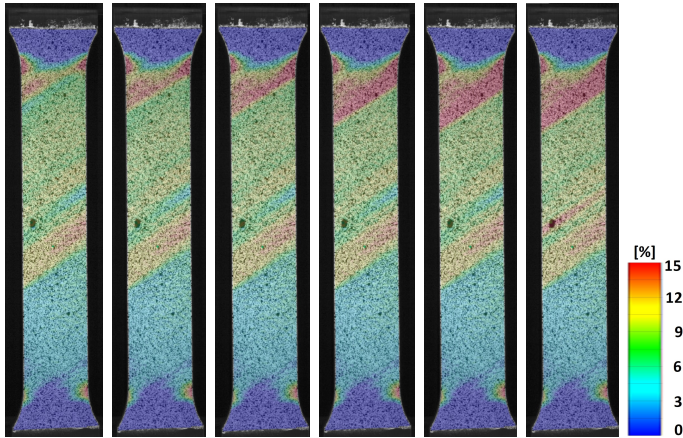


FIG. 16. Evolution of longitudinal engineering strains for experimental sample 5 (medium strain rate) in time steps numbered from left to right.

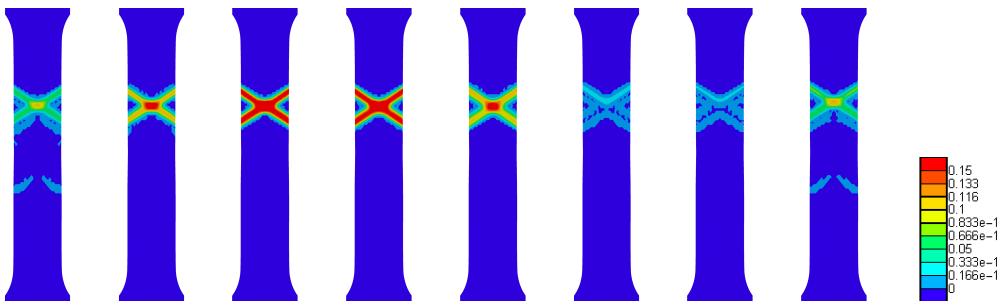


FIG. 17. Distribution of equivalent plastic strain rate $\dot{\alpha}$ in selected steps (marked by red points in Fig. 15).

of the serration, the cross shear band pattern becomes distinct and stabilises as can be seen in images numbers 3 and 4. It then starts to vanish at the local force minimum and almost disappears on the local re-hardening branch (images number 6 and 7). In the last image, associated with the next local peak in the right diagram of Fig. 15, the shear band pattern becomes distinct again due to recurring instability. The first and the last images, plotted for the adjacent peaks, are similar, although a very small translation of the localised plastic strain pattern upwards can be noticed in the last image. Then the process repeats. It can be noticed that serration amplitudes are similar for the experiments and computations, see Fig. 15, but the distances between the peaks are different.

In Figs. 18 and 19 further experimental results are presented. The distributions of temperature and strain measure (longitudinal engineering strain) are

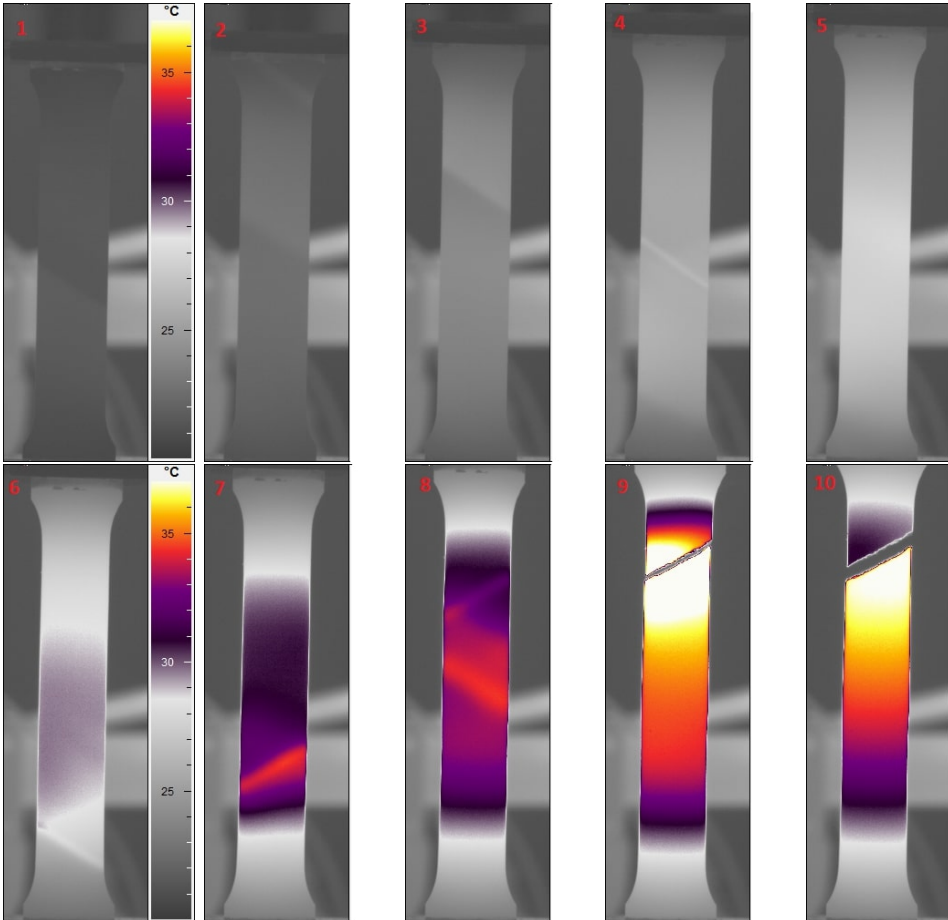


FIG. 18. Evolution of temperature for experimental sample 5 (medium strain rate) in equal intervals of 5.2 s.

respectively shown for the sample number 5 (medium strain rate) in equal intervals of 5.2 s. The images in Fig. 19 are rotated 90 degrees clockwise with respect to the orientation chosen in Fig. 18 (i.e. the top of the sample is on the right). It is recalled that the experiments were performed at room temperature (20–21 degrees Celsius). Localised temperature bands can be observed during the whole process, see images number 4, 6, 7 and 8 in Fig. 18. A V-shape band pattern can be observed in image number 6, whereas X-shape patterns are not visible. The shear bands can be inclined upwards or downwards, cf. images number 6 and 8. The band inclination with respect to the transverse x -axis (in Fig. 9 coordinate y refers to the longitudinal axis) for the failure mode is approximately 30 degrees, see also Fig. 7 where the failure mode is shown. During the process the inclination can be larger, see image number 6 in Fig. 18, where the band inclination angle is closer to 35 degrees.

The maximum temperature rise in the sample is between 10 and 20 degrees. Close to final failure the temperature increases significantly in the proximity of the crack. Shear bands can be also observed in the DIC images of the longitudinal

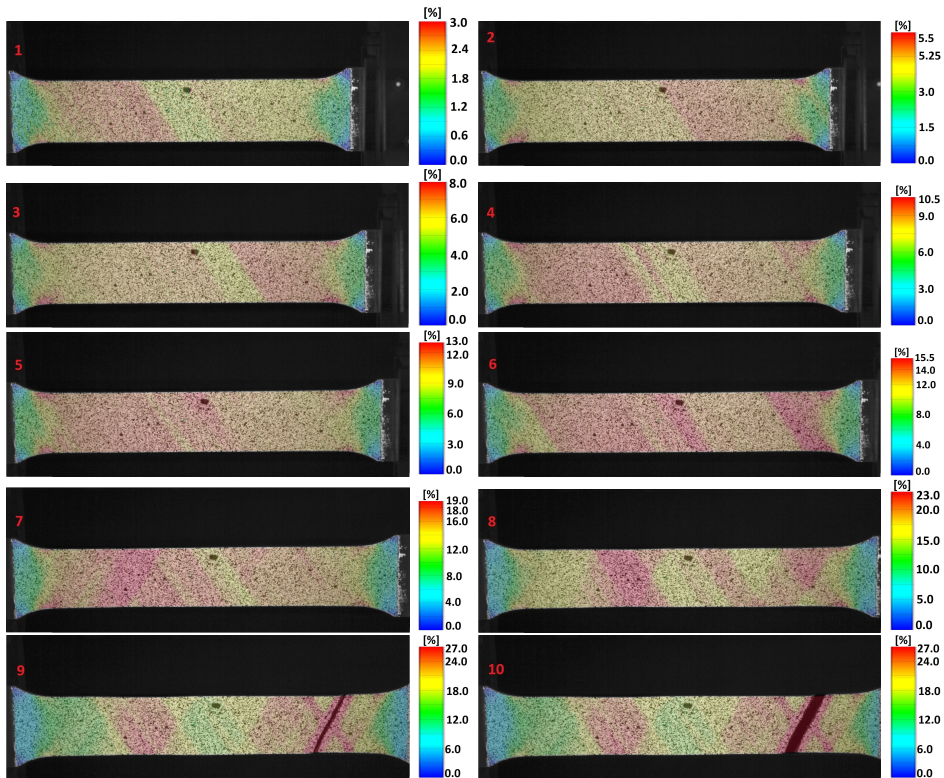


FIG. 19. Evolution of engineering strain for experimental sample 5 (medium strain rate) in equal intervals of 5.2 s.

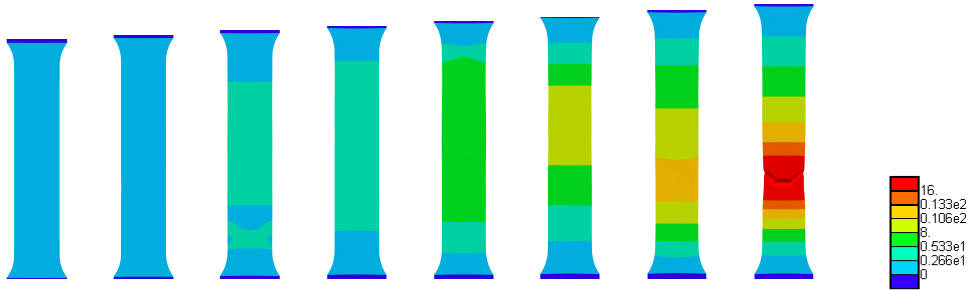


FIG. 20. Evolution of temperature for medium strain rate in equal intervals of 5.2 s (from left to right).

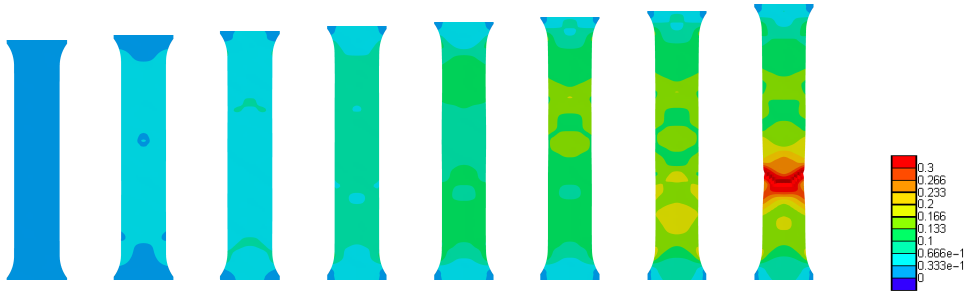


FIG. 21. Evolution of longitudinal engineering strain for medium strain rate in equal intervals of 5.2 s.

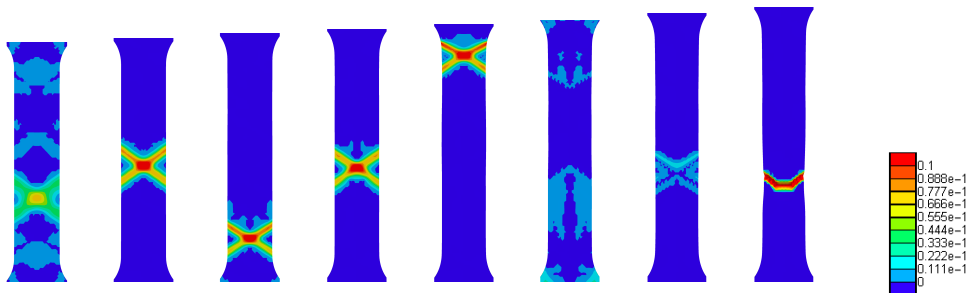


FIG. 22. Evolution of α for medium strain rate in equal intervals of 5.2 s.

engineering strain presented in Fig. 19. For an advanced plastic process these images are similar to the distributions of accumulated plastic strain measure. The images mostly exhibit single tilted bands but X-shape band patterns can also be spotted as in images number 8 (in the right part of the sample), 9 and 10.

The next three figures present the results of simulations performed with the thermo-visco-plastic model. In Fig. 20 the distribution of relative temperature (ΔT) is displayed in equal intervals of 5.2 s (the last two pictures are skipped because image number 8 already shows the predicted failure mode). The sample is inhomogeneously heated due to plastic dissipation in regions where shear bands appear. However, due to the high conductivity of aluminium, heat is quickly distributed and not many bands can be spotted during the process. Only in the third image from the left an X-shape band pattern is visible (which can also be seen in Fig. 22). Localisation of temperature is visible in the two images from the right, at the place where the final band pattern is formed. The temperature increases in the sample by 16 to 20 degrees, which is not far from the experimental outcome.

In Fig. 21 the distribution of longitudinal engineering strain is displayed in equal intervals of 5.2 s (again the last two pictures are skipped). Non-homogeneous deformation can be observed throughout the simulated process. Shear bands can be spotted in images number 3, 5, 6, 7 and 8 (from left). The strain levels are quite similar to the experiments, see Fig. 19. In the images it is not easy to figure out where a currently active band is located. To resolve this problem, in Fig. 22 the distribution of the rate of equivalent plastic strain $\dot{\alpha}$ is displayed. As in the previous figures the images are plotted in equal intervals of 5.2 s (the last two pictures are skipped). These images are used to observe where the process is active in a current time step. Due to symmetry, moving or appearing and disappearing X-shape band patterns are visible in the sample rather than the single tilted bands seen in the experiments. In some time steps more than one active plastic zone is distinguishable. The inclination of the bands is approximately 30–35 degrees which is compatible with the experimental findings (the inclination is measured in the current configuration). In the experimental results the failure mode is brittle and in computations a V-shape band pattern is visible, followed by necking, see Fig. 19 (experiments) and 21 (computations). The final localisation places also differ, for experiments they are in the top part of the sample and for computations in the bottom part.

5. Conclusions

Propagative instabilities observed in experiments for aluminium alloy AW5083 have been compared with their numerical simulations. Bone-shape samples in tension loaded under three strain rates have been tested at room temperature. Equipment which can monitor both the displacement and temperature fields has been used. Two employed large strain thermo-visco-plastic models (without and with gradient enhancement), upgraded with special switch functions, can replicate Lueders bands and the PLC effect behaviour in one process. Integral, local and field data obtained in the experiments and simulations are

compared, including force–displacement diagrams, temperature at the central point of the sample model (in current configuration) and images showing the distributions of the longitudinal engineering strain and temperature. Special attention is paid to the detailed assessment of the two propagating instability phenomena. Therefore, images of the computed equivalent plastic strain rate are additionally examined to visualise the evolution of instabilities.

The simulations are able to represent the Lueders-type response at the beginning of the process and the PLC serrations in the hardening phase of the response. The results show a good agreement between force–displacement diagrams (up to the failure mode) and temperature levels observed for the laboratory specimens and simulated configurations. Some material model parameters have been manually tuned to the experimental results for the medium strain rate, so that the results for this case show the closest agreement. The numerical model should be improved to obtain a better fit of the results for a broad range of strain rates. Mesh sensitivity has not been a part of this research since the models are regularised.

At the beginning of the plastic process, both in the experiments and computations, two localised strain zones (one in the bottom part, one in the top part of the sample) representing the Lueders phenomenon can be observed. In the experiments only one tilted band is observed, but in computations due to symmetry (both the boundary conditions and the mesh are symmetric) two X-shape band patterns appear. Plastic fronts formed at the edges of the bands then move towards each other due to hardening and finally merge.

The PLC stage of the loading process is too unstable to be reproduced numerically with such accuracy as the Lueders bands, although the recurring shear bands related to serrations behave in a similar way (move or appear and disappear in a repetitive manner) in the experiments and simulations. The magnitudes of serrations and the inclinations of the shear bands in experiments and computations are also comparable.

The main differences are visible in the failure modes. In the experimental samples failure is brittle along an inclined line and in the computations necking is observed. The moment when the failure occurs does not seem to be fully controlled. In experiments it is driven by micro-structure defects and in computations by an additional switch function and numerical imperfections. The temperature averaging, employed as additional regularisation, seems to have no significant influence on the presented results due to small temperature gradients. However, for higher strain rates, when local temperature variation is large due to semi-adiabatic conditions, it could play a more significant role. Moreover, the interaction of the location of the failure zone with the location of initial Lueders bands and, respectively or, the PLC effect dominated band locations is of interest for future research.

There are a few ways to enhance the computational model. Firstly, to obtain a better fit of computations to experiments a full parameter identification should be performed. For this purpose, experiments performed on a notched specimen could be useful both in experiments and numerical modelling by setting the place where the first band is formed. Identification may be extended by the analysis of strain variations in for instance dog-bone type specimens, i.e. differences in strain levels within and outside bands, and consideration of different strain contributions such as principal strains and shear strains. Secondly, the model could be augmented by incorporation of thermo-elastic coupling which represents the Gough–Joule effect, which is visible when the experimental results are analysed. Thirdly, some further model improvements, for instance the introduction of McCormick model parameters depending on temperature, should be examined. This would require experiments to be performed for different temperatures, especially as it is known that the propagative instability phenomena depend not only on the strain rate, but also on temperature. Finally, different options of gradient enhancement could be considered to further examine the issue of regularisation in the context of propagative instabilities.

Acknowledgements

The research was supported by the National Science Centre of Poland within the grant number 2018/31/N/ST8/03573.

Appendices

A. Aspects of thermodynamic consistency

From the first and second law of thermodynamics, the Clausius–Planck inequality can be obtained. Following the Coleman–Noll procedure of rational thermodynamics, the mechanical dissipation reduces to

$$(A.1) \quad \mathcal{D}_{\text{mech}} = \boldsymbol{\tau} : \mathbf{d}^P + h \dot{\alpha} \geq 0$$

with internal hardening variable α and the associated driving force $h = -\partial\psi/\partial\alpha$. To prove thermodynamic consistency, the chosen evolution equations for the plastic part of the symmetric velocity gradient \mathbf{d}^P and for the hardening variable are inserted in Eq. (A.1). The evolution of the symmetric part of the plastic velocity gradient is related to the evolution of the elastic left Cauchy–Green deformation tensor via

$$(A.2) \quad -\frac{1}{2}\mathcal{L}_v \mathbf{b}^e = \dot{\gamma} \mathbf{N}^p \mathbf{b}^e = \text{sym}(\mathbf{l}^p \mathbf{b}^e),$$

see, e.g., [60]. Assuming an isotropic plastic flow, in addition to the elastically isotropic response, makes the plastic part of the spatial velocity gradient symmetric, i.e. $\mathbf{l}^p = \mathbf{d}^p$, and coaxial with \mathbf{b}^e so that

$$(A.3) \quad -\frac{1}{2}\mathcal{L}_v \mathbf{b}^e = \dot{\gamma} \mathbf{N}^p \mathbf{b}^e = \mathbf{d}^p \mathbf{b}^e \implies \mathbf{d}^p = \dot{\gamma} \mathbf{N}^p = \dot{\gamma} \frac{\partial F_p}{\partial \boldsymbol{\tau}}$$

with the direction of the plastic flow as defined in Section 3.1. Moreover, the evolution of the internal hardening variable is assumed as

$$(A.4) \quad \dot{\alpha} = \sqrt{\frac{2}{3}} \dot{\gamma},$$

cf. Section 3.1. Inserting evolution equations (A.3) and (A.4) into the reduced dissipation inequality (A.1) yields

$$(A.5) \quad \mathcal{D}_{\text{mech}} = \dot{\gamma} \left[\boldsymbol{\tau} : \frac{\partial F_p}{\partial \boldsymbol{\tau}} + \sqrt{\frac{2}{3}} h \right].$$

Before showing that this expression for the dissipation satisfies the second law of thermodynamics, i.e. is always larger or equal to zero, the yield function F_p and the plastic Helmholtz energy ψ^p are considered in order to reformulate Eq. (A.5) and bring it into a more suitable format.

The only contribution of the yield surface F_p which depends on the Kirchhoff stress $\boldsymbol{\tau}$ is the equivalent Huber–Mises–Hencky stress measure $f(\boldsymbol{\tau})$, see Eq. (3.7), which is homogeneous of degree one in the Kirchhoff stress, so that

$$(A.6) \quad \boldsymbol{\tau} : \frac{\partial F_p}{\partial \boldsymbol{\tau}} = \boldsymbol{\tau} : \frac{\partial f}{\partial \boldsymbol{\tau}} = f.$$

The plastic free energy ψ^p is the only contribution in the free energy function which depends on the internal hardening variable α and represents the amount of energy which is stored e.g. in plastic lattice deformations. Although different definitions could be adopted without influencing the actual material response from a purely material modelling point of view, a standard expression for linear and exponential hardening, i.e.

$$(A.7) \quad \psi^p = \frac{1}{2} H \alpha^2 + [\sigma_{yf} - \sigma_{y0}] \left[\alpha + \frac{1}{\delta} \exp(-\delta \alpha) \right],$$

is chosen here to prove thermodynamic consistency of the model. It is worth mentioning that this part provides an almost arbitrary adjustment capability, but choosing an ansatz identical to standard approaches will result in a similar free energy being stored due to similar hardening processes if compared to standard

models. From the free energy, the driving force of the internal hardening variable directly follows as

$$(A.8) \quad h = -\frac{\partial\psi}{\partial\alpha} = -\frac{\partial\psi^p}{\partial\alpha} = -[H\alpha + [\sigma_{yf} - \sigma_{y0}][1 - \exp(-\delta\alpha)]].$$

Concerning the dissipation inequality, it is now possible to use Eqs. (A.6) and (A.8) in (A.5) to obtain

$$(A.9) \quad \mathcal{D}_{\text{mech}} = \dot{\gamma} \left[f - \sqrt{\frac{2}{3}} [H\alpha + [\sigma_{yf} - \sigma_{y0}][1 - \exp(-\delta\alpha)]] \right].$$

There are only two possible states for the model at hand, either the process is elastic so that the plastic multiplier as well as the mechanical dissipation vanish, i.e. $\dot{\gamma} = 0$ and $\mathcal{D}_{\text{mech}} = 0$, or the process is inelastic and the current stress state is restricted to lie on the yield surface. Such an inelastic process results in

$$(A.10) \quad F_p = f - \sqrt{\frac{2}{3}} [\sigma_H + \sigma_V + \sigma_B] = 0 \iff f = \sqrt{\frac{2}{3}} [\sigma_H + \sigma_V + \sigma_B].$$

Using this relation in the dissipation relation (A.9) leads to

$$(A.11) \quad \mathcal{D}_{\text{mech}} = \sqrt{\frac{2}{3}} \dot{\gamma} [\sigma_H + \sigma_V + \sigma_B - H\alpha - [\sigma_{yf} - \sigma_{y0}][1 - \exp(-\delta\alpha)]].$$

Inserting the respective contributions introduced in Section 3.1 and two additional definitions to simplify the presentation, we obtain

$$(A.12) \quad \mathcal{D}_{\text{mech}} = \sqrt{\frac{2}{3}} \dot{\gamma} \left[[\sigma_{y0} + S_1(\alpha)H\alpha + S_2(\alpha)S_3(\alpha) \overbrace{[\sigma_{yf} - \sigma_{y0}]}^{\Delta\sigma_y}] \right. \\ \left. \times [1 - \exp(-\delta\alpha)] \overbrace{[1 - H_T[T - T_0]]}^{\vartheta(T) \in [0,1]} \right. \\ \left. + \sigma_V + \sigma_B - H\alpha - [\sigma_{yf} - \sigma_{y0}][1 - \exp(-\delta\alpha)] \right]$$

$$(A.13) \quad = \sqrt{\frac{2}{3}} \dot{\gamma} \left[\vartheta(T)\sigma_{y0} + \vartheta(T)S_1(\alpha)H\alpha + \vartheta(T)S_2(\alpha)S_3(\alpha)\Delta\sigma_y \right. \\ \left. \times [1 - \exp(-\delta\alpha)] + \sigma_V + \sigma_B - H\alpha - \Delta\sigma_y[1 - \exp(-\delta\alpha)] \right]$$

$$(A.14) \quad = \sqrt{\frac{2}{3}} \dot{\gamma} \left[\overbrace{\vartheta(T)\sigma_{y0}}^{\in [0,1]} - H\alpha \overbrace{[1 - \vartheta(T)S_1(\alpha)]}^{\geq 0} + \overbrace{[\vartheta(T)S_2(\alpha)S_3(\alpha) - 1]}^{\in [0,1]} \right. \\ \left. \times \Delta\sigma_y \overbrace{[1 - \exp(-\delta\alpha)]}^{\in [0,1]} + \underbrace{\sigma_V}_{\geq 0} + \underbrace{\sigma_B}_{\geq 0} \right].$$

It can now be seen that the terms associated with linear softening $H\alpha$ (with $H < 0$), viscosity σ_V and the DSA phenomenon σ_B are not critical, i.e. these respective contributions do not violate the second law of thermodynamics. The only part which could be negative is the one associated with exponential hardening including $\Delta\sigma_y$. Hence the model is guaranteed to be thermodynamically consistent if

$$(A.15) \quad \vartheta(T)\sigma_{y0} + [\vartheta(T)S_2(\alpha)S_3(\alpha) - 1]\Delta\sigma_y \geq 0,$$

assuming the maximum value 1 for the factor $[1 - \exp(-\delta\alpha)]$ of the critical, negative addend. The minimum value (in α) of the left hand side of this relation is obtained when either $S_2 = 0$ or $S_3 = 0$, which results in

$$(A.16) \quad \vartheta(T)\sigma_{y0} - \Delta\sigma_y \geq 0.$$

Hence, thermodynamic consistency of the model at hand can be ensured for a chosen temperature interval if

$$(A.17) \quad \vartheta(T) = \underbrace{1 - H_T[T - T_0]}_{\in[0,1]} \geq \frac{\Delta\sigma_y}{\sigma_{y0}} = \frac{\sigma_{yf} - \sigma_{y0}}{\sigma_{y0}} = \frac{\sigma_{yf}}{\sigma_{y0}} - 1$$

$$\iff 2 - H_T[T - T_0] \geq \frac{\sigma_{yf}}{\sigma_{y0}},$$

i.e. if the material parameter for thermal softening is chosen in relation to the initial and saturation hardening limits. More precisely speaking, the saturation limit may, at the most, be twice as high as the initial yield limit and the maximum admissible ratio decreases with the increasing temperature range $[T - T_0]$ and with the increasing (positive) thermal softening parameter H_T .

It is worth mentioning that the maximum admissible temperature range for the material parameters chosen in this work (cf. Table 2), is $T - T_0 = 170.45$ K.

B. Local material response

In order to show the local homogeneous response the proposed model predicts, the simulation of a cubic sample discretised with one finite element is performed. The cube of dimensions $L = 5$ mm, $S = 10$ mm, $H = 5$ mm, see Fig. 23, is extended by an enforced displacement growing to $\Delta L = 2.5$ mm. Mechanical essential boundary conditions allow for uniform deformation and thermal insulation is assumed on the whole surface of the cube.

The simulation is performed using the same code and material parameters as in Section 4. Moreover, the area of the cross section perpendicular to the tension direction is consistent with the analysed dog-bone sample. In order to obtain

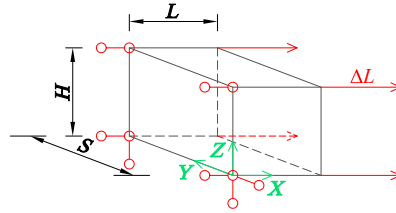


FIG. 23. Homogeneous deformation – geometry and mechanical boundary conditions (in red).

the medium average strain rate, i.e. $4.3 \cdot 10^{-3}$ 1/s, the duration of the elongation process is assumed to be $t_{MAX} = 115$ s.

The obtained diagrams presenting the sum of reactions F vs sample elongation d are shown in Fig. 24. The onset of the plastic process is followed by a very short softening phase (hardly visible in the diagram but confirmed in the numerical output) and a plateau which smoothly transforms into saturation hardening. In the second half of the elongation process the material undergoes softening. The application of switch $S_3(\alpha)$ incorporating the arctan function prevents the force F from decreasing to zero in the final part of the simulation.

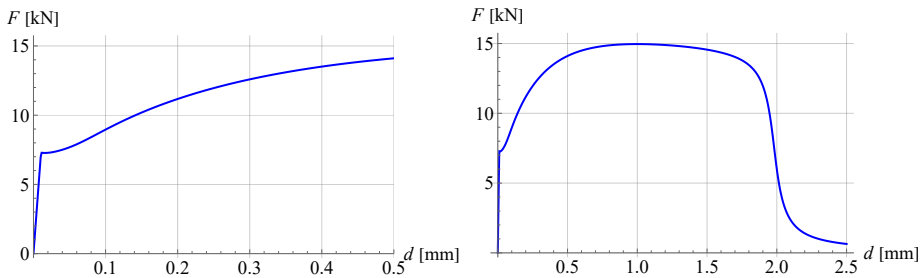


FIG. 24. Sum of reactions vs sample elongation for the initial part of the process (left) and the entire simulation (right).

The comparison of the force–displacement relation with the diagram of the Kirchhoff stress measure $f(\boldsymbol{\tau})$ from Eq. (3.6), see Fig. 25, shows the influence of geometrical softening on the overall response of the specimen. The stress measure $f(\boldsymbol{\tau})$ begins to decrease significantly later than the total reaction force, shortly after the hardening variable reaches value α_1 . During the plastic process small thermal softening is also present due to temperature increase, see Fig. 26.

Taking the results for the homogeneous response into account it should be emphasised that the force–displacement diagram is smooth and does not reproduce serrations characteristic for the PLC effect.

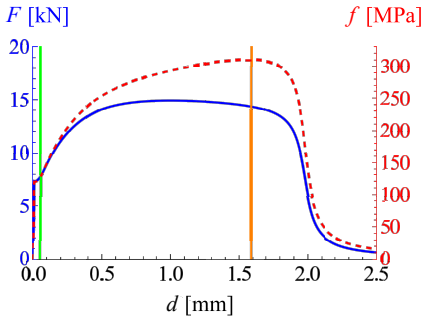


FIG. 25. Sum of reactions (in blue) and stress measure (in red) vs sample elongation. Green and orange vertical lines indicate stages when hardening variable α reaches values α_{LB} and α_1 , respectively.

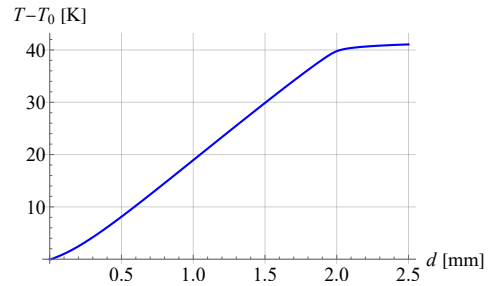


FIG. 26. Temperature increase vs sample elongation.

References

1. Y. BERGSTROM, W. ROBERTS, *The application of dislocation model to dynamic strain ageing in α -iron containing interstitial atoms*, *Acta Metallurgica*, **19**, 815–823, 1971.
2. P.G. MCCORMIC, *Theory of flow localization due to dynamic strain aging*, *Acta Metallurgica*, **36**, 12, 3061–3067, 1988.
3. W. LÜDERS, *Über die Äusserung der Elasticität an stahlartigen Eisenstäben und Stahlstäben, und über eine beim Biegen solcher Stäbe beobachtete Molecularbewegung*, *Dingler's Polytechnisches Journal*, **5**, 18–22, 1860.
4. M.O. EREMIN, A.O. CHIRKOV, M.V. NADEZHKIN, L.B. ZUEV, *Microstructure-based finite-difference analysis of the plastic flow in low-carbon steel*, *European Journal of Mechanics - A/Solids*, **93**, article 104531, 2022.
5. A. PORTEVIN, F. LE CHATELIER, *Sur un phénomène observé lors de l'essai de traction d'alliages en cours de transformation*, *Comptes rendus de l'Académie des Sciences*, **176**, 507–510, 1923.
6. A. KOZŁOWSKA, B. GRZEGORCZYK, M. MORAWIEC, A. GRAJCAR, *Explanation of the PLC effect in advanced high-strength medium-Mn steels. A review*, *Materials*, **12**, 24, 1–14, 2019.
7. A.H. COTTRELL, B.A. BILBY, *Dislocation theory of yielding and strain ageing of iron*, *Proceedings of the Physical Society. Section A*, **62**, 1, 49–62, 1949.
8. A.H. COTTRELL, *A note on the Portevin–Le Chatelier effect*, *The London, Edinburgh, and Dublin Philosophical Magazine and Journal of Science*, **44**, 829–832, 1953.
9. H.B. SUN, F. YOSHIDA, X. MA, T. KAMEI, M. OHMORI, *Finite element simulation on the propagation of Lüders band and effect of stress concentration*, *Materials Letters*, **57**, 21, 3206–3210, 2003.
10. J. COËR, P.-Y. MANACH, H. LAURENT, M.C. OLIVEIRA, L.F. MENEZES, *Piobert–Lüders plateau and Portevin–Le Chatelier effect in an Al–Mg alloy in simple shear*, *Mechanics Research Communications*, **48**, 1–7, 2013.

11. M. MAZIÈRE, C. LUIS, A. MARAIS, S. FOREST, M. GASPÈRINI, *Experimental and numerical analysis of the Lüders phenomenon in simple shear*, International Journal of Solids and Structures, **106–107**, 305–314, 2017.
12. S. KYRIAKIDES, A. OK, E. CORONA, *Localization and propagation of curvature under pure bending in steel tubes with Lüders bands*, International Journal of Solids and Structures, **45**, 10, 3074–3087, 2008.
13. J.F. HALLAI, S. KYRIAKIDES, *On the effect of Lüders bands on the bending of steel tubes. Part I: Experiments*, International Journal of Solids and Structures, **48**, 3275–3284, 2011.
14. J.F. HALLAI, S. KYRIAKIDES, *On the effect of Lüders bands on the bending of steel tubes. Part II: Analysis*, International Journal of Solids and Structures, **48**, 3285–3298, 2011.
15. G. SINGH, T. NANDA, S.J. MIADAD, N.C. GORAIN, T. VENUGOPALAN, B.R. KUMAR, *Correlation between Lüders band formation and precipitation kinetics behaviour during the industrial processing of interstitial free high strength steels*, Archives of Civil and Mechanical Engineering, **19**, 2, 469–483, 2019.
16. X.G. WANG, B.B. HE, C.H. LIU, C. JIANG, M.X. HUANG, *Extraordinary Lüders-strain-rate in medium Mn steels*, Materialia, **6**, 100288, 2019.
17. D.J. LLOYD, L.R. MORRIS, *Luders band deformation in a fine grained aluminium alloy*, Acta Metallurgica, **25**, 8, 857–861, 1977.
18. Y.-L. CAI, S.-L. YANG, S.-H. FU, Q.-C. ZHANG, *The influence of specimen thickness on the Lüders effect of a 5456 Al-based alloy: experimental observations*, Metals, **6**, 5, 1–12, 2016.
19. M. REZAAE-HAJIDEHI, S. STUPKIEWICZ, *Gradient-enhanced model and its micromorphic regularization for simulation of Lüders-like bands in shape memory alloys*, International Journal of Solids and Structures, **135**, 208–218, 2018.
20. B.S. SHARIAT, Y. LI, H. YANG, Y. WANG, Y. LIU, *On the Lüders band formation and propagation in NiTi shape memory alloys*, Journal of Materials Science & Technology, **116**, 22–29, 2022.
21. Y. CHOI, J. HA, M.-G. LEE, Y.P. KORKOLIS, *Observation of Portevin–Le Chatelier effect in aluminum alloy 7075-W under a heterogeneous stress field*, Scripta Materialia, **205**, article 114178, 2021.
22. Z. HU, Y. QI, X. NIE, H. ZHANG, H. ZHU, *The Portevin–Le Chatelier (PLC) effect in an Al-Cu aluminum alloy fabricated by selective laser melting*, Materials Characterization, **178**, article 111198, 2021.
23. J. MIN, J. LIN, B. SUN, *Effect of strain rate on spatio-temporal behavior of Portevin–Le Chatelier bands in a twinning induced plasticity steel*, Mechanics of Materials, **68**, 164–175, 2014.
24. A. SARKAR, S.A. MALOY, K.L. MURTY, *Investigation of Portevin–Le Chatelier effect in HT-9 steel*, Materials Science and Engineering: A, **631**, 120–125, 2015.
25. X. HUANG, X. ZHOU, W. WANG, C. CUI, H. YE, Z. YANG, *Influence of microtwins on Portevin–Le Chatelier effect of a Ni-Co based disk superalloy*, Scripta Materialia, **209**, article 114385, 2022.
26. N.A. SENE, P. BALLAND, K. BOUABDALLAH, *Experimental study of Portevin–Le Chatelier bands on tensile and plane strain tensile tests*, Archives of Civil and Mechanical Engineering, **18**, 94–102, 2018.

27. P.-Y. MANACH, S. THUILLIER, J.W. YOON, J. COËR, H. LAURENT, *Kinematics of Portevin–Le Chatelier bands in simple shear*, International Journal of Plasticity, **58**, 66–83, 2014.
28. B. SKOCZEŃ, J. BIELSKI, J. TABIN, *Multiaxial constitutive model of discontinuous plastic flow at cryogenic temperatures*, International Journal of Plasticity, **55**, 198–218, 2014.
29. J. XU, G. CHEN, S. FU, *Complexity analysis of the Portevin–Le Chatelier in an Al alloy at different temperatures*, Theoretical and Applied Mechanics Letters, **11**, 2, article 100233, 2021.
30. B. REYNE, P.-Y. MANACH, N. MOËS, *Macroscopic consequences of Piobert–Lüders and Portevin–Le Chatelier bands during tensile deformation in Al-Mg alloys*, Materials Science and Engineering: A, **746**, 11, 187–196, 2019.
31. S.C. REN, T.F. MORGENEYER, M. MAZIÈRE, S. FOREST, G. ROUSSELIER, *Effect of Lüders and Portevin–Le Chatelier localization bands on plasticity and fracture of notched steel specimens studied by DIC and FE simulations*, International Journal of Plasticity, **136**, article 102880, 2021.
32. A. YILMAX, *The Portevin–Le Chatelier effect: a review of experimental findings*, Science and Technology of Advanced Materials, **12**, 6, 2011.
33. W.M. WANG, *Stationary and Propagative Instabilities in Metals – a Computational Point of View*, PhD dissertation, Delft University of Technology, Delft, 1997.
34. M. MUCHA, B. WCISŁO, J. PAMIN, *Simulation of PLC effect using regularized large strain elasto-plasticity*, Materials, **15**, 12, 21 pp., article 4327, 2022.
35. P.G. MCCORMICK, C.P. LING, *Numerical modelling of the Portevin–Le Chatelier effect*, Acta Metallurgica et Materialia, **43**, 5, 1969–1977, 1995.
36. S. ZHANG, P.G. MCCORMICK, Y. ESTRIN, *The morphology of Portevin–Le Chatelier bands: finite element simulation for Al-Mg-Si*, Acta Materialia, **49**, 6, 1087–1094, 2001.
37. T. BÖHLKE, G. BONDÁR, Y. ESTRIN, M.A. LEBYODKIN, *Geometrically non-linear modeling of the Portevin–Le Chatelier effect*, Computational Materials Science, **44**, 4, 1076–1088, 2009.
38. B. KLUSEMANN, G. FISCHER, T. BÖHLKE, B. SVENDSEN, *Thermomechanical characterization of Portevin–Le Chatelier bands in AlMg3 (aa5754) and modeling based on a modified Estrin–McCormick approach*, International Journal of Plasticity, **67**, 192–216, 2015.
39. L.Z. MANSOURI, S. THUILLIER, P.-Y. MANACH, *Thermo-mechanical modeling of Portevin–Le Chatelier instabilities under various loading paths*, International Journal of Mechanical Sciences, **115**, 676–688, 2016.
40. P. HÄHNER, E. RIZZI, *On the kinematics of Portevin–Le Chatelier bands: theoretical and numerical modelling*, Acta Materialia, **51**, 12, 3385–3397, 2003.
41. E. RIZZI, P. HÄHNER, *On the Portevin–Le Chatelier effect: theoretical modeling and numerical results*, International Journal of Plasticity, **20**, 1, 121–165, 2004.
42. M. MAZIÈRE, J. BESSON, S. FOREST, B. TANGUY, H. CHALONS, F. VOGEL, *Numerical aspects in the finite element simulation of the Portevin–Le Chatelier effect*, Computer Methods in Applied Mechanics and Engineering, **199**, 9, 734–754, 2010.

43. B. WCISŁO, J. PAMIN, *Local and non-local thermomechanical modeling of elastic-plastic materials undergoing large strains*, International Journal for Numerical Methods in Engineering, **109**, 1, 102–124, 2017.
44. J. PAMIN, B. WCISŁO, K. KOWALCZYK-GAJEWSKA, *Gradient-enhanced large strain thermoplasticity with automatic linearization and localization simulations*, Journal of Mechanics of Materials and Structures, **12**, 1, 123–146, 2017.
45. M. MUCHA, B. WCISŁO, J. PAMIN, *Simulation of Lueders bands using regularized large strain elasto-plasticity*, Archives of Mechanics, **73**, 1, 83–117, 2021.
46. J. KORLEC, *Automation of the Finite Element Method*, [in:] P. Wriggers, editor, Nonlinear finite element methods, pages 483–508, Springer-Verlag, Berlin Heidelberg, 2008.
47. J.C. SIMO, C. MIEHE, *Associative coupled thermoplasticity at finite strains: Formulation, numerical analysis and implementation*, Computer Methods in Applied Mechanics and Engineering, **98**, 1, 41–104, 1992.
48. P.A. WRIGGERS, C. MIEHE, M. KLEIBER, J.C. SIMO, *On the coupled thermomechanical treatment of necking problems via finite element methods*, International Journal for Numerical Methods in Engineering, **33**, 869–883, 1992.
49. J. KORLEC, P. WRIGGERS, *Automation of Finite Element Methods*, Springer International Publishing Switzerland, Switzerland, 2016.
50. S. FOREST, E. LORENTZ, *Localization phenomena and regularization methods*, [in:] J. Besson [ed.], Local Approach to Fracture, pp. 311–370, Les Presses de l'École des Mines, Paris, 2004.
51. J. LEMONDS, A. NEEDLEMAN, *Finite element analyses of shear localization in rate and temperature dependent solids*, Mechanics of Materials, **5**, 339–361, 1986.
52. R.C. BATRA, C.H. KIM, *Effect of thermal conductivity on the initiation, growth and bandwidth of adiabatic shear bands*, International Journal of Engineering Science, **29**, 8, 949–960, 1991.
53. A. NEEDLEMAN, *Material rate dependence and mesh sensitivity in localization problems*, Computer Methods in Applied Mechanics and Engineering, **67**, 69–86, 1988.
54. J. C. SIMO, *Strain softening and dissipation: a unification of approaches*, [in:] J. Mazars, Z.P. Bažant [eds.], Cracking and Damage: Strain Localization and Size Effect, pp. 440–461, York, Elsevier Applied Science, London, New York, 1989.
55. W.M. WANG, L.J. SLUYS, R. DE BORST, *Viscoplasticity for instabilities due to strain softening and strain-rate softening*, International Journal for Numerical Methods in Engineering, **40**, 20, 3839–3864, 1997.
56. B. WCISŁO, J. PAMIN, K. KOWALCZYK-GAJEWSKA, *Gradient-enhanced damage model for large deformations of elastic-plastic materials*, Archives of Mechanics, **65**, 5, 407–428, 2013.
57. E.A. DE SOUZA NETO, D. PERIC, D.R.J. OWEN, *Computational methods for plasticity. Theory and applications*, John Wiley & Sons, Chichester, UK, 2008.
58. ALLOYS INTERNATIONAL, inc., <https://alloysintl.com/>. Accessed: 2021-11-17.
59. G.I. TAYLOR, H. QUINNEY, *The latent energy remaining in a metal after cold working*, Proceedings of the Royal Society A, **143**, 307–326, 1934.

60. A. MENZEL, P. STEINMANN, *On the spatial formulation of anisotropic multiplicative elasto-plasticity*, Computer Methods in Applied Mechanics and Engineering, **192**, 3431–3470, 2003.

Received November 30, 2022; revised version March 2, 2023.

Published online June 21, 2023.
